7-21-2014

Digital anthropomorphic phantoms of non-rigid human respiratory and voluntary body motion for investigating motion correction in emission imaging

Arda Könik
University of Massachusetts Medical School

Caitlin M. Connolly
Beth Israel Deaconess Medical Center

Karen L. Johnson
University of Massachusetts Medical School

Paul Dasari
University of Massachusetts Medical School

Paul W. Segars
Duke University Medical Center

See next page for additional authors

Recommended Citation

Könik, A., Connolly, C., Johnson, K., Dasari, P., Segars, P., Pretorius, P., Lindsay, C., Dey, J., & King, M. (2014). Digital anthropomorphic phantoms of non-rigid human respiratory and voluntary body motion for investigating motion correction in emission imaging. *Physics in Medicine and Biology, 59* (14), 3669-3682. https://doi.org/10.1088/0031-9155/59/14/3669

Published in final edited form as:
Phys Med Biol. 2014 July 21; 59(14): 3669–3682. doi:10.1088/0031-9155/59/14/3669.

Digital Anthropomorphic Phantoms of Non-Rigid Human Respiratory and Voluntary Body Motion for Investigating Motion Correction in Emission Imaging

Arda Könik[1], **Caitlin M Connolly**[2], **Karen L Johnson**[1], **Paul Dasari**[1,3], **Paul W Segars**[4], **P H Pretorius**[1], **Clifford Lindsay**[5], **Joyoni Dey**[1], and **Michael A King**[1]

[1]Department of Radiology, University of Massachusetts Medical School, Worcester, MA

[2]Department of Radiology, Beth Israel Deaconess Medical Center, Boston, MA

[3]Department of Biomedical Engineering, Worcester Polytechnic Institute, Worcester, MA

[4]Department of Radiology, Duke University Med. Center, Durham, NC

[5]Department of Computer Science, Worcester Polytechnic Institute, Worcester, MA

Abstract

The development of methods for correcting patient motion in emission tomography has been receiving increased attention. Often performance of these methods is evaluated through simulations using digital anthropomorphic phantoms, such as the commonly used XCAT phantom, which models both respiratory and cardiac motion based on human studies. However, non-rigid body motion, which is frequently seen in clinical studies, is not present in the standard XCAT phantom. In addition, respiratory motion in the standard phantom is limited to a single generic trend. In this work, to obtain more realistic representation of motion, we developed a series of individual-specific XCAT phantoms modeling non-rigid respiratory and non-rigid body motions derived from the MRI acquisitions of volunteers. Acquisitions were performed in the sagittal orientation using the Navigator methodology. Baseline (no motion) acquisitions at end-expiration were obtained at the beginning of each imaging session for each volunteer. For the body motion studies, MRI was again acquired only at end-expiration for five body motion poses (shoulder stretch, shoulder twist, lateral bend, side roll, and axial slide). For the respiratory motion studies, MRI was acquired during free/regular breathing. The MR slices were then retrospectively sorted into 14 amplitude-binned respiratory states, end-expiration, end-inspiration, six intermediary states during inspiration, and six during expiration using the recorded Navigator signal. XCAT phantoms were then generated based on these MRI data by interactive alignment of the organ contours of the XCAT with the MRI slices using a GUI. Thus far we have created 5 body motion and 5 respiratory motion XCAT phantoms from MRI acquisitions of 6 healthy volunteers (3 males and 3 females). Non-rigid motion exhibited by the volunteers was reflected in both respiratory and body motion phantoms with a varying extent and character for each individual. In addition to these phantoms, we recorded the position of markers placed on the chest of volunteers for the body motion studies, which could be used as external motion measurement. Using these phantoms and external motion data, investigators will be able to test their motion correction approaches for

arda.konik@umassmed.edu.

realistic motion obtained from different individuals. The NURBS data and the parameter files for these phantoms are freely available for downloading and can be used with the XCAT license.*

Keywords

Respiratory and body motion; motion correction; XCAT phantoms; PET; SPECT

1. Introduction

Patient respiratory and body motions are inevitable during the scan time of emission tomography studies. These motions introduce an additional source of blurring and artifacts to the SPECT and PET reconstructions due to inconsistent projection data, and a mismatch between emission data and attenuation maps employed for attenuation correction Alessio *et al* 2010, McQuaid and Hutton 2008). A number of methods have been developed to detect and correct for body and respiratory motion using emission data (O'Connor *et al* 1998, Kyme *et al* 2003, Dawood *et al* 2008, Gilland *et al* 2002) or information from external tracking devices (Bloomfield *et al* 2003, Bruyant *et al* 2005, Barnes *et al* 2008, McNamara *et al* 2009, Buther *et al* 2009, Mukherjee *et al* 2009).

The effectiveness of motion correction methods applied to emission tomography can be tested in different ways. **Physical phantoms** in most cases are rigid (e.g., Data Spectrum Anthropomorphic Phantom), and thus do not reflect true non-rigid nature of patient motion although relatively flexible phantoms have also been constructed (Fieseler *et al* 2011). **Patient Studies** are the ultimate way to test the correction methods. However, knowing the ground truth is often not possible. Also, they are expensive to collect and validate. Further they are good only for existing imaging systems and cannot be used to evaluate a new design. **Mathematical phantoms** based on simple geometrical constructs provide the ground truth and can be simulated in computer environment without needing expensive nuclear medicine devices. These phantoms can vary from a simple cylindrical phantom with a cyclic linear motion (Murase *et al* 1987) to more complicated ones with geometric structures representing human anatomy such as widely used Mathematical Cardiac Torso (MCAT) phantom, which was later modified to include cardiac (Pretorius *et al* 1999) and respiratory motion models (Segars *et al* 2001). While mathematical phantoms provide quick validations and proof of principle, they are usually far from representing in detail real patient anatomy and motion. A more advanced approach is to use **Realistic computerized phantoms** based on actual human anatomy and physiology. Commonly, these phantoms are constructed using non-uniform rational B-spline (NURBS) surfaces, which enable accurate representations of complex organ shapes in the segmentation process of the patient images (Lee *et al* 2007). In nuclear medicine, the best known and widely used phantom in this category is the NURBS-based cardiac torso (NCAT) (Segars 2001), which is considered as the next-generation MCAT (Tsui and Segars 2009) because of its much more realistic organ shapes that are based 3D Visible Human CT dataset (Tsui and Segars 2009). The latest generation of these phantoms, the extended cardiac torso (XCAT) phantom (Segars *et al* 2008, Segars *et al* 2010) provided even more anatomical details. A detailed evolution of these phantoms from MCAT to XCAT was described in (Tsui and Segars 2009), and further

extension of the XCAT phantoms for larger populations, which used the same cardiac and respiratory motion mechanics (Segars *et al* 2013). Coupled with Monte Carlo tools such as GATE (Jan *et al* 2004), SIMIND (Ljungberg and Strand, 1989), and SimSET (Harrison) or analytical tools to accurately simulate the imaging system, these phantoms have been used to create datasets for studying the effect of motion and testing reconstruction algorithms that employ motion correction (Park *et al* 2011).

The XCAT phantom provides realistic representation of the human anatomy and physiological functions including cardiac and respiratory motion models based on real human data. However, non-rigid body motion that is frequently observed in clinical studies is not included in the standard XCAT phantom. In addition, respiratory motion is limited to a single general trend observed from patient CT datasets (Segars *et al* 2008), which does not reflect the non-rigid organ motion. Several different approaches can be found in the literature to obtain more realistic respiratory motion. For example Mishra et al (Mishra *et al* 2012), have developed a modified version of the XCAT phantom allowing irregular breathing patterns, which also incorporated lung tumor motion from recorded patient studies. To simulate PET-MR acquisitions in the presence of respiratory motion, Tsoumpas et al (Tsoumpas *et al* 2011) have created realistic 4D PET image datasets from the segmentation of acquired MRI data directly, without using any intermediary mathematical phantom.

In this investigation, we developed a series of individual-specific XCAT phantoms modeling non-rigid respiratory (14 time frames) and non-rigid body motions (6 different postures including baseline) based on MRI acquisitions of volunteers. We also recorded the position of markers placed on the chest of volunteers for usage in simulating external surrogates for the body motion studies and superior-inferior displacements of the liver dome for the non-rigid respiratory motion studies. To our knowledge, this is the first time XCAT phantoms were created to model non-rigid body motions, which also included external marker data. In addition, as opposed to a single respiratory motion trend defined by a set of equations provided by the standard XCAT phantom, we created a series of respiratory phantoms from five volunteers. Using these phantoms and the external motion information, investigators will be able to test their body and respiratory motion correction approaches (e.g., motion tracking, respiratory binning, iterative reconstruction, etc.) in various realistic conditions provided by different individuals.

The NURBS and corresponding marker data for these phantoms are freely available for downloading for usage by investigators with the XCAT license. Therefore, the users will have the flexibility to change the activity distributions and emission energies for their specific SPECT or PET simulations. The methods for creating the XCAT phantoms, as well as the details of MRI acquisitions are presented in the next section.

2. Methods

2.1. MRI Acquisitions

Under Institutional Review Board (IRB) approval and informed consent, MRI of volunteers was performed with a 3.0-T whole body scanner (Philips Healthcare, the Netherlands) using

the built-in quadrature body coil. All scans were performed without the use of contrast agents. During imaging the volunteers were in the supine position with arms over their head as in a classical SPECT cardiac perfusion imaging. Five spherical markers of 2 cm diameter filled with copper sulfate solution were placed on the volunteers' chest for visualization in the MRI. For body motion studies, these markers were included in the list of structures for which NURBS-surfaces were created. These markers can thus be used to provide external tracking information as could be provided by a visual-tracking system (McNamara *et al* 2009). The MR images of the torso of each volunteer were acquired in sagittal orientation employing acquisition parameters of 2D T1-Fast Field Echo, TR / TE = 5.5 ms / 3.1 ms and voxel size =3 mm.

The Navigator method (Ehman and Felmlee 1989) was employed to control / determine the respiratory state during which acquisition occurred. To do this the Navigator box was centrally placed at the liver and lung boundary allowing us to track the 1D respiratory motion in superior-inferior direction as shown in figure 1. The Navigator method was used in two different ways in this work. For baseline and body motion studies, MRI was acquired only during end-expiration as determined by having the signal from the Navigator within an acceptance window to minimize any respiratory contribution to the motion. For the respiratory motion studies, MRI was acquired during free breathing, and the recorded Navigator signal was used for the retrospective sorting of the slices into a sequence of respiratory states. The signal from a pneumatic bellows on the abdomen of the patients was also recorded during all MRI.

The next three sub-sections describe the MRI acquisition methods we employed for baseline, body motion, and respiratory motion studies in more detail.

2.2. Baseline (No Motion)

As an initial step for both respiratory and body motion studies, we acquired an end-expiration baseline (no motion) MRI state for each volunteer with ~120 sagittal slices (thickness: 3 mm) across the torso. The number of slices varied depending on the size of the volunteer. Typically the acquisition took 20-40 minutes depending on how well the volunteer maintained their respiratory signal within the Navigator acceptance window.

2.3. Body Motion

Following the baseline acquisition, several body motion-states simulating clinically noted motions (Mukherjee *et al* 2010), were acquired with the same acquisition parameters as described above, except that slices had 3 mm gaps between them to reduce the acquisition time by half. These body motion-states were:

- Axial slide – an approximately rigid-body caudal shift in body position
- Lateral torso bend – a bend laterally to one side at the shoulder level while maintaining the position of the hips
- Shoulder twist – a rotation at the shoulder level while maintaining the position of the hips

- Shoulder stretch – a superior extension of the left arm
- Side roll – a rolling of the entire torso

The volunteers maintained their postures for each of these motion-states during each MRI acquisition. In three of the studies, the order of motion states was: shoulder stretch, axial slide, side roll, shoulder twist and lateral bend. In the remaining two studies the order was: shoulder stretch, shoulder twist, lateral bend, side roll and axial slide.

2.4. Respiratory Motion

MRI acquisitions for respiratory motion were different from the body motion acquisitions, and were performed with a separate set of volunteers. For each volunteer, between 45 to 52 dynamic MRI acquisitions were performed at ~50 slice locations across the torso during free breathing (three studies had 3 mm gaps as in the body motion studies and 2 studies without gaps). This provided up to 52 individual sagittal slices at different respiratory time points for each slice location. These slices were then sorted into a complete respiratory cycle (separate bins for inspiration and expiration) using the amplitude signals from the pressure bellow placed on the abdomen (for 3 volunteer studies) or the displacement of the Navigator marker placed on the dome of the liver (for 2 volunteer studies). With up to 52 dynamic acquisitions during free-breathing for a given slice position, there were often multiple choices (or sometimes no choice) when retrospective binning was employed to form 3D slices sets for a given amplitude bin. For example, to obtain 14 respiratory frames from a 50 slice × 45 dynamics study, 2250 slices were available to fill 14 × 50 = 700 slices. When this slice degeneracy occurred, our algorithm chose the slice with the amplitude value closest to the mid-point in that amplitude bin. The process of retrospective binning of a 50 slice × 45 dynamics acquisition is illustrated in figure 2 with 7 equally separated amplitude bins, which corresponds to 14 time frames obtained over the respiratory cycle (7 inspiration + 7 expiration). Once the MRI slices were sorted into a respiratory cycle forming 4D MRI datasets, they were used to build the 4D XCAT phantoms as detailed in the next section.

2.5. Creating XCAT Phantom Motion States

The next step after MRI acquisitions was to create individual-specific XCAT phantoms using an interactive graphical user interface (GUI) developed by Dr. Segars, which allowed the users to manually adapt the NURBS-based structures of the XCAT phantom to the tomographic data (in this case MRI) in axial, coronal and sagittal slices. A portion of the GUI showing the 3D rendering of the NURBS organ surfaces and axial MRI slice from the baseline acquisition (gapless) with the corresponding NURBS organ outlines overlaid and two of the markers contoured, is presented in figure 3.

The fitting of the XCAT to MRI was done by first contouring the body shape, followed by scaling the skeleton to match the volunteer's skeleton, and then shaping each organ to match the MRI data by moving the control points of NURBS. The baseline phantom was built first since the gapless MR images facilitate the fitting process. Then the baseline XCAT phantom was deformed to obtain the motion phantoms using the associated volunteer MRI data as templates. All the organs were deformed non-rigidly to reflect the true motion of the body, except for the baseline heart, which was transformed rigidly (6-DOF). For body motion

studies, chest markers seen in the MR slices were also included as NURBS structures as can be seen in figure 3. For the respiratory motion studies, while the marker data was available, we did not segment them as NURBS structures. Instead, the 1D-Navigator displacement data and bellows data are available as external measurements.

Finally, using Dr. Segar's licensed program (dxcat1), NURBS data were converted to voxelized activity and attenuation phantoms based on the user-defined parameters of relative organ concentrations of activity and the energy of the photons emitted.

3. Results

Thus far we have created 5 body motion XCAT phantoms and 5 respiratory motion XCAT phantoms from MRI acquisitions of 6 healthy volunteers (3 males and 3 females). Four of the volunteers participated in both body and respiratory motion studies, which were performed on separate days.

In figure 4, an example body motion study is presented. The 1st row shows the MRI slices in coronal orientation for the 6 different postures. The 2nd row shows the corresponding XCAT voxelized slices (overlaid attenuation and emission maps) modeling the ^{99m}Tc Sestamibi distribution with the following relative activity concentrations (activity/voxel): Left ventricle 75, right ventricle 65, left atrium 50, right atrium 40, liver 75, kidney 75, spleen 75, gall bladder 60, lungs 4, bones 10 and background 10. The 3rd row shows the extent of body motion with respect to baseline (baseline - motion state) of the XCAT attenuation slices. The 4th row shows the rendered images of these phantoms to illustrate the full volumetric body motion. Note that the sternum was made semi-transparent for illustration purposes and cartilage is absent since it was not modeled in this study as could not be seen in the MRI slices.

For each volunteer study, the extent of motion varied. Using a registration program (Dey *et al* 2010) we obtained the 6-DOF motion of the heart, liver and spleen with respect to the baseline. The rotation (degree) and translation (mm) values for the 5 volunteer studies and 5 motion states are listed in Table I, where right-left (RL), anterior-posterior (AP) and superior-inferior (SI) directions are indicated with positive-negative signs, respectively. Note, while the volunteers tried to return to their baseline before performing the next motion state, one can expect to see residual motions from previous motion states. This is one of the reasons why for two of the volunteers a considerable amount of motion in RL and AP are noted even in the case of axial slide, which was not the 1st motion state following the baseline. Also, apart from the residual motion, volunteers might have moved differently from the intended motion.

In figure 5, a volunteer study for the respiratory motion (from end-inspiration to end-expiration) is shown. The relatively smooth organ boundaries seen on the MR coronal images (first row) indicate that respiratory amplitude binning of the sagittal slices (acquired at separate times) is in good agreement despite minor imperfections. The trend of respiration can be seen with the aid of the line drawn across the liver dome. XCAT voxelized slices (overlaid attenuation and emission maps) obtained from this retrospectively sorted MR data

are shown in the 2nd row, and the difference attenuation images in the 3rd row, where the dark and bright lung contours indicate the SI motion of the liver and heart. 4th row shows the rendered XCAT phantoms illustrating the volumetric respiratory motion.

A unique respiratory cycle for each volunteer was observed. In Figure 6, the SI displacements calculated from the center of mass of the organs (heart, liver, and spleen), as well as volume changes in the left lung (right lung followed a similar trend) for 14 time frames (start-inspiration to end-expiration) are presented.

4. Discussion

We have created XCAT phantoms based on the individual-specific respiratory and body motions obtained from MRI of volunteers. The body motion phantoms include markers (available in the XCAT parameter file) on the chest to serve as external surrogates for internal motion.

In our earlier approach, MRI acquisitions were performed with ECG gating to “freeze” the beating heart. However, ECG gating prolonged acquisitions limiting the number of respiratory cycles that could be acquired. This limited our ability to acquire an adequate number of slices to fill the amplitude bins for the various respiratory states. In addition, volunteers tend to change their respiratory pattern and potentially perform body motions during prolonged studies (~ 40 minutes), which further complicates the binning process. Also their heart rate typically drifted during the protracted imaging time further complicating acquisition. We therefore, eliminated the ECG gating to increase the imaging sampling rate. With this approach, we managed to obtain up to 4 times higher sampling rate, which allowed us to obtain sagittal slices without 3 mm gaps twice fast. Another improvement in our approach was to use the Navigator marker located at the lung-liver boundary (figure 1). This provides more precise motion information compared to the external measurements obtained from the abdomen bellow as we had previously employed (Konik *et al* 2012).

A drawback of our method is that manual segmenting is time consuming and requires expert knowledge of human anatomy. Additionally, segmentation in two-dimensional MRI slices and interpolating into three-dimensional structures can lead to interpolation artifacts. To address these issues, a semi-automated method is being developed (Lindsay *et al* 2012). However, rib segmentation remains challenging because of the lack of MRI bone contrast compared to lung. In addition, cartilage was not included in these models as it cannot be differentiated with our MRI methods. However, the electron density of cartilage and soft tissue are not very different (du Plessis *et al* 1998). Thus its presence would not alter the attenuation considerably in this region, expecially for photon energies higher than 100 keV.

In another study creating non-rigid respiratory motion datasets from MRI acquisitions (Tsoumpas *et al* 2011), the investigators have generated high-resolution 4D MRI datasets combining the information obtained from dynamic acquisitions (similar to the method described here), and high-resolution static MRI acquisition. The motion fields obtained from the dynamic dataset were applied to the static dataset to obtain high-resolution 4D MRI

dataset, which was then segmented to model PET activity and attenuation distributions to employ in PET-MR simulations. A limitation they mentioned in their method was the absence of the bone in the segmentation. In our method, using the existing anatomy of XCAT phantoms, we were able to align the skeleton and the ribs to the MRI slices based on where the blank regions appeared in the MRI slices. For example, rib locations can be identified from the repeating blank regions in coronal MRI slices shown in the first rows of figure 4 and 5.

We expect that these phantoms will serve as a valuable tool in simulation studies investigating motion correction and registration approaches in PET and SPECT imaging. In fact, they are already being used in different projects among our group members. For example, the body motion phantoms were used in the development of a registration algorithm for cardiac SPECT employing both primary and scatter windows (Dey *et al* 2012). In another application, these phantoms were used in SIMIND simulations for investigation of data-driven body motion correction strategies (Mukherjee *et al* 2012). The respiratory motion XCAT phantoms can be used for investigating respiratory motion correction approches in more realistic conditions where organs move non-rigidly and follow different patterns during inspiration and expiration. Other than motion studies, the baseline phantoms could also be used for simulation applications for anatomical variations in 6 different individuals.

5. Conclusion

We have developed XCAT non-rigid body and non-rigid respiratory motion phantoms based on the MRI acquisitions of volunteers, and asssociated external marker information, which were not available features in the standard XCAT phantoms. Using these phantoms and the external tracking information, investigators will be able to test their motion correction approaches for realistic motion in different individuals. All the data including MRI datasets, NURBS files, and the parameter files for these phantoms are freely available for downloading[1] and can be used with the XCAT license[2].

Acknowledgments

This work was supported by the National Institute of Biomedical Imaging and Bioengineering (NIBIB) grant R01 EB001457 and a research grant from Philips Healthcare. The contents are solely the responsibility of the authors and do not represent the official views of the NIBIB or Philips Healthcare.

This work is a continuation of investigations previously partially reported at the 2011 SPIE Meeting as: Connolly CM, Konik A, Dasari PKR, Segars P, Zheng S, Johnson KL, Dey J, King MA. Creation of 3D Digital Anthropomorphic Phantoms which Model Actual Patient Non-rigid Body Motion as Determined from MRI and Position Tracking Studies of Volunteers. Proceedings of SPIE Conference 7964, pp79642G1-8, 2011; and further at the 2011 IEEE Nuclear Science Symposium and Medical Imaging Conference as: Konik A, Connolly CM, Johnson KL, Dasari P, Segars WP, Pretorius PH, King MA. Digital Anthropomorphic Phantoms of Non-Rigid Human Respiratory and Voluntary Body Motions: A Tool-Set for Investigating Motion Correction in 3D Reconstruction. Proceedings of 2011 IEEE Medical Imaging Conference, MIC17-2, 2011.

[1]Contact Dr. Arda Könik for the datasets (arda.konik@umassmed.edu)
[2]Contact Dr. Paul W. Segars for the XCAT license (paul.segars@duke.edu)

References

Alessio AM, Kinahan PE, Champley KM, Caldwell JH. Attenuation-emission alignment in cardiac PET/CT based on consistency conditions. Med Phys. 2010; 37:1191–200. [PubMed: 20384256]

Barnes PJ, Baldock C, Meikle SR, Fulton RR. Benchmarking of a motion sensing system for medical imaging and radiotherapy. Phys Med Biol. 2008; 53:5845–57. [PubMed: 18827318]

Bloomfield PM, Spinks TJ, Reed J, Schnorr L, Westrip AM, Livieratos L, Fulton R, Jones T. The design and implementation of a motion correction scheme for neurological. PET Phys Med Biol. 2003; 48:959–78.

Bruyant PP, Gennert MA, Speckert GC, Beach RD, Morgenstern JD, Kumar N, Nadella S, King MA. A Robust Visual Tracking System for Patient Motion Detection in SPECT: Hardware Solutions. IEEE Trans Nucl Sci. 2005; 52:1288–94. [PubMed: 19081772]

Buther F, Dawood M, Stegger L, Wubbeling F, Schafers M, Schober O, Schafers KP. List mode-driven cardiac and respiratory gating in PET. J Nucl Med. 2009; 50:674–81. [PubMed: 19372491]

Dawood M, Buther F, Jiang X, Schafers KP. Respiratory motion correction in 3-D PET data with advanced optical flow algorithms. IEEE Trans Med Imaging. 2008; 27:1164–75. [PubMed: 18672433]

Dey J, Konik A, Segars WP, King MA. Multi-modal Rigid and Non-Rigid Registration for Attenuation Correction in Cardiac SPECT/CT using Emission Scatter to CT conversion. IEEE NSS/MIC. 2012:2859–66.

Dey J, Segars WP, Pretorius PH, Walvick RP, Bruyant PP, Dahlberg S, King MA. Estimation and correction of cardiac respiratory motion in SPECT in the presence of limited-angle effects due to irregular respiration. Med Phys. 2010; 37:6453–65. [PubMed: 21302801]

du Plessis FCP, Willemse CA, Lotter MG, Goedhals L. The indirect use of CT numbers to establish material properties needed for Monte Carlo calculation of dose distributions in patients. Medical Physics. 1998; 25:1195–201. [PubMed: 9682205]

Ehman RL, Felmlee JP. Adaptive technique for high-definition MR imaging of moving structures. Radiology. 1989; 173:255–63. [PubMed: 2781017]

Fieseler M, Koesters T, Gigengack F, Braun H, Quick HH, Schaefers KP, Jiang X. Motion correction in PET-MRI: A human torso phantom study. IEEE NSS/MIC. 2011:3586–88.

Gilland DR, Mair BA, Bowsher JE, Jaszczak RJ. Simultaneous reconstruction and motion estimation for gated cardiac ECT. iEEE Transactions on Nuclear Science. 2002; 49:2344–49.

Harrison, RL. Simulation System for Emission Tomography. http://depts.washington.edu/simset/html/simset_main.html

ICRU. Tissue substitutes in radiation dosimetry and measurement ICRU Report. 1989. p. 44

Jan S, et al. GATE: a simulation toolkit for PET and SPECT. Phys Med Biol. 2004; 49:4543–61. [PubMed: 15552416]

Konik A, et al. Respiratory Tracking Using EDR for List-Mode Binning in Cardiac Emission Tomography:Comparison with MRI Heart Motion Measurements. IEEE-MIC. 2012 (Anneheim.

Kyme AZ, Hutton BF, Hatton RL, Skerrett DW, Barnden LR. Practical aspects of a data-driven motion correction approach for brain SPECT. IEEE Trans Med Imaging. 2003; 22:722–9. [PubMed: 12872947]

Lee C, Lodwick D, Hasenauer D, Williams JL, Lee C, Bolch WE. Hybrid computational phantoms of the male and female newborn patient: NURBS-based whole-body models. Phys Med Biol. 2007; 52:3309–33. [PubMed: 17664546]

Lindsay, K.; Gennert, MA.; Connolly, C.; Konik, A.; Dasari, P.; Segars, WP.; King, MA. SPIE. San Diego, CA: 2012. Interactive Generation of Digital Anthropomorphic Phantoms from XCAT Shape Priors.

Ljungberg M, Strand SE. A Monte Carlo program for the simulation of scintillation camera characteristics. Comp Meth Prog Biomed. 1989; 29:257–72.

McNamara JE, Pretorius PH, Johnson K, Mukherjee JM, Dey J, Gennert MA, King MA. A flexible multicamera visual-tracking system for detecting and correcting motion-induced artifacts in cardiac. SPECT slices Med Phys. 2009; 36:1913–23.

McQuaid SJ, Hutton BF. Sources of attenuation-correction artefacts in cardiac PET/CT and SPECT/CT. Eur J Nucl Med Mol Imaging. 2008; 35:1117–23. [PubMed: 18219483]

Mishra P, James SS, Segars WP, Berbeco RI, Lewis JH. Adaptation and applications of a realistic digital phantom based on patient lung tumor trajectories. Phys Med Biol. 2012; 57:3597–608. [PubMed: 22595980]

Mukherjee, JM.; Dey, J.; Konik, A.; Hutton, BF.; King, MA. A comparison of data-driven methods for patient motion estimation in cardiac SPECT imaging. presented at IEEE-MIC; Anaheim, CA. 2012; 2012.

Mukherjee JM, Johnson KL, McNamara JE, King MA. Quantitative Study of Rigid-Body and Respiratory Motion of Patients Undergoing Stress and Rest Cardiac SPECT Imaging. IEEE Trans Nucl Sci. 2010; 57:1105–15. [PubMed: 20694041]

Mukherjee JM, McNamara JE, Johnson KL, Dey J, King MA. Estimation of Rigid-Body and Respiratory Motion of the Heart From Marker-Tracking Data for SPECT Motion Correction. IEEE Trans Nucl Sci. 2009; 56:147–55. [PubMed: 20539825]

Murase K, Ishine M, Kataoka M, Itoh H, Mogami H, Lio A, Hamamoto K. Simulation and experimental study of respiratory motion effect on image quality of single photon emission computed tomography (SPECT). Eur J Nucl Med. 1987; 13:244–49. [PubMed: 3499324]

O'Connor MK, Kanal KM, Gebhard MW, Rossman PJ. Comparison of four motion correction techniques in SPECT imaging of the heart: a cardiac phantom study. J Nucl Med. 1998; 39:2027–34. [PubMed: 9867136]

Park, MJ.; Chen, S.; Lee, T-S.; Fung, GSK.; Lodge, M.; Tsui, BMW. Generation and Evaluation of a Simultaneous Cardiac and Respiratory Gated Rb-82 PET Simulation. IEEE NSS/MIC Conference Record; 2011. p. 3327-30.

Pretorius PH, King MA, Tsui BMW, LaCroix KJ, Xia W. A mathematical model of motion of the heart for use in generating source and attenuation maps for simulating emission imaging. Med Phys. 1999; 26:2323–32. [PubMed: 10587213]

Segars, WP. Development of a new dynamic NURBS-based cardiac-torso (NCAT) phantom. The University of North Carolina; May. 2001 2001

Segars WP, et al. Population of anatomically variable 4D XCAT adult phantoms for imaging research and optimization. Med Phys. 2013; 40

Segars WP, Lalush DS, Tsui BMW. Modeling respiratory mechanics in the MCAT and spline-based MCAT phantoms. IEEE Trans Nucl Sci. 2001; 48:89–97.

Segars WP, Mahesh M, Beck TJ, Frey EC, Tsui BM. Realistic CT simulation using the 4D XCAT phantom. Med Phys. 2008; 35:3800–8. [PubMed: 18777939]

Segars WP, Sturgeon G, Mendonca S, Grimes J, Tsui BM. 4D XCAT phantom for multimodality imaging research. Med Phys. 2010; 37:4902–15. [PubMed: 20964209]

Tsoumpas C, et al. Fast generation of 4D PET-MR data from real dynamic MR acquisitions. Phys Med Biol. 2011; 56:6597–613. [PubMed: 21937775]

Tsui B, Segars WP. MCAT to XCAT: The Evolution of 4-D Computerized Phantoms for Imaging Research. Proceedings of the IEEE. 2009; 97:1954–68.

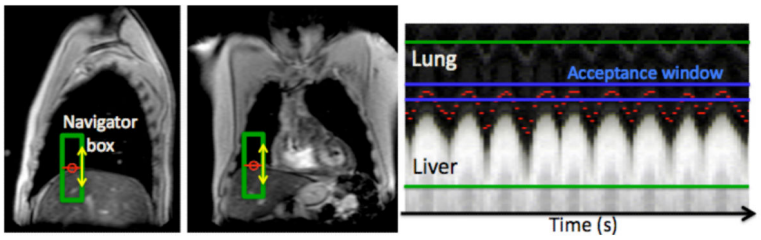

Figure 1.

(Left and Center) Navigator box is shown on the dome of the liver in sagittal and coronal MRI slices. (Right) For the baseline and body motion MRI acquisitions, the slices were recorded only at end-expiration, when the liver/lung boundary detected by the Navigator method (indicated by dashed marks) was within the acceptance window (interval between the lines). In contrast, for the respiratory motion studies, MRI was acquired without using the acceptance window.

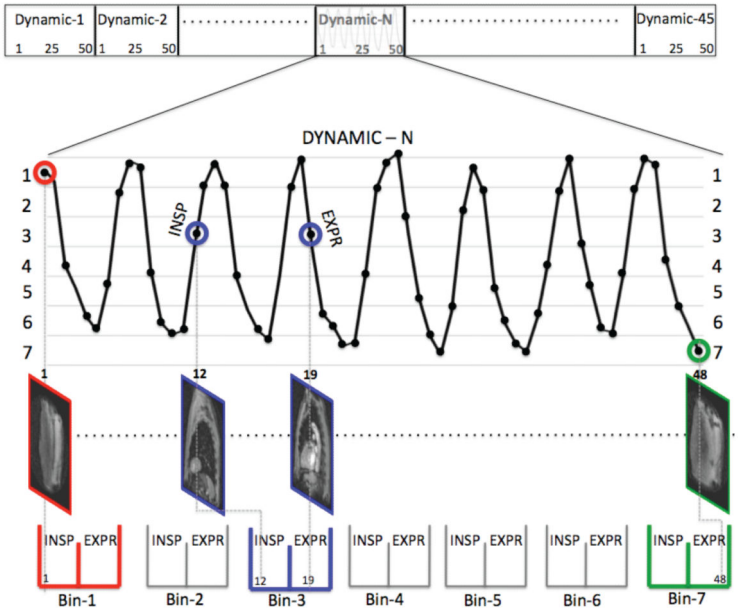

Figure 2.

Illustration of retrospective binning of 45 MRI acquisitions (Dynamic-1 to Dynamic-45) of 50 slices across the torso performed during free breathing. Dynamic-N is shown as an example. Sagittal slices were placed into 7 equally separated respiratory bins based on the amplitude of their Navigator or bellows signals. These slices are then sorted into inspiration and expiration phases. The sorting of four slices (1, 12, 19 and 48) into bin-1 (end-inspiration), into bin-3 (inspiration and expiration), and into bin-7 (end-expiration) is illustrated. This procedure was followed for all 45 dynamics. When multiple slice candidates occurred for a given slice position and bin, the slice with the amplitude value closest to the mid-point was selected.

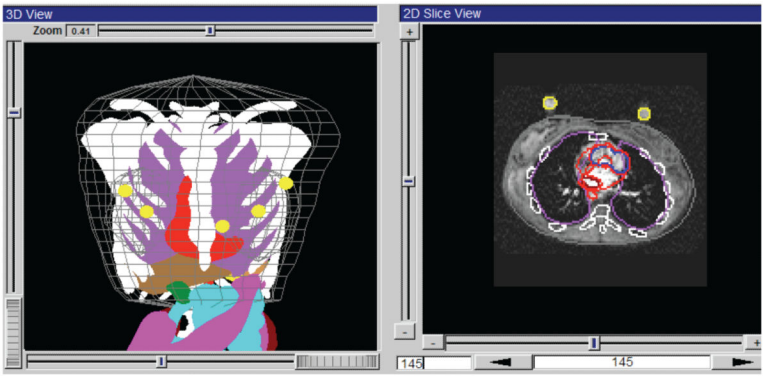

Figure 3.

Shown is a portion of the GUI used to create NURBS-based XCAT phantoms. (Left) 3D rendering of the NURBS organ surfaces and the 5 spherical markers placed on the chest. (Right) A transverse MRI slice with NURBS organ outlines overlaid and two of the markers contoured. The user forms the NURBS organs and markers by contouring the boundaries in the MRI slices using the orientation and scaling tools (not shown) in the GUI.

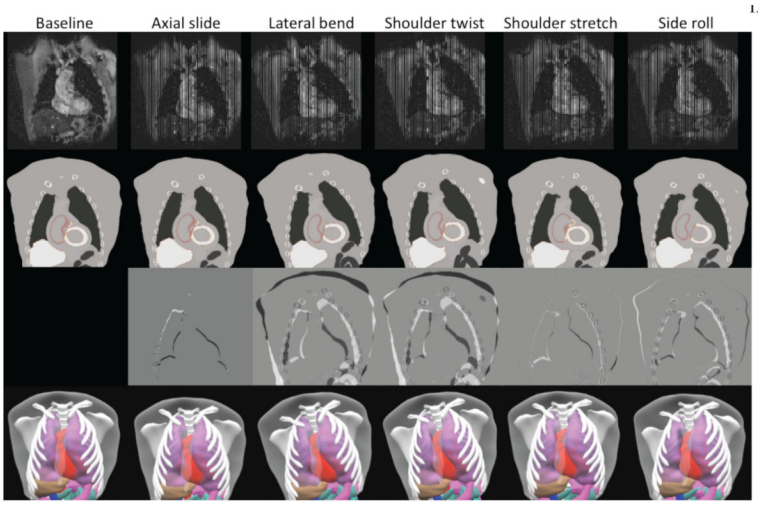

Figure 4.

An example XCAT body-motion volunteer study for 6 different postures. 1st row: MRI coronal slices. Except for the baseline, all the MRI motion studies have 3 mm gaps between acquisitions of 3 mm thick sagittal slices. 2nd row: Corresponding XCAT coronal slices (attenuation + emission) for a ^{99m}Tc Sestamibi distribution. 3rd row: Difference images of attenuation between baseline and motion postures showing the extent of motion with respect to baseline image (1st column is empty since baseline - baseline is zero). 4th row: Rendered XCAT phantoms. The sternum is displayed as semi-transparent to allow better visualization of the heart.

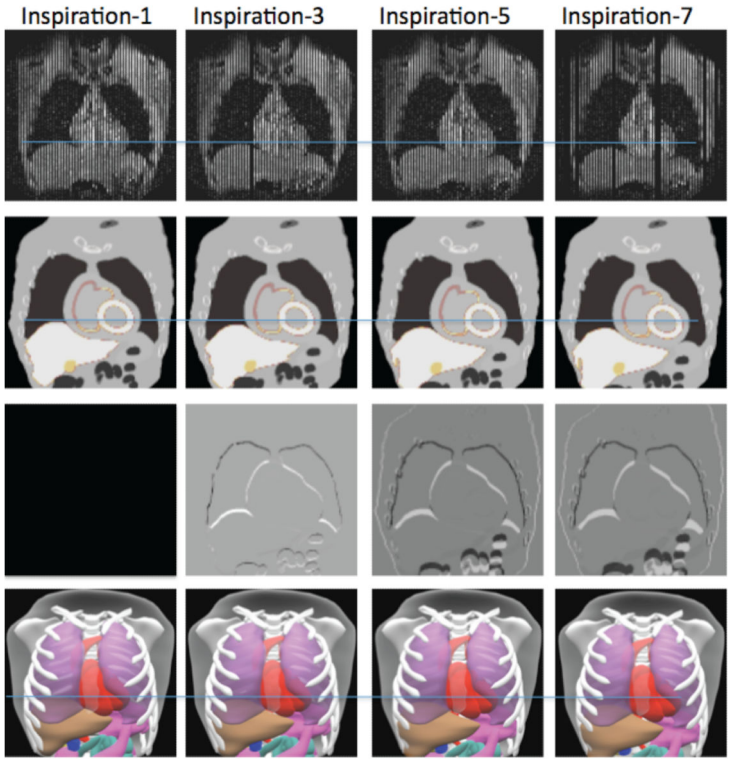

Figure 5.

An example XCAT respiratory motion volunteer study showing inspiration bins, 1, 3, 5 and 7. 1st row: MRI slices were acquired in sagittal orientation and sorted into the amplitude bins (coronal slice shown). Combining all the sagittal slices forms the 3D MRI for each time frame, or all together 4D MRI data set. The respiratory trend can be seen with the aid of the blue lines running horizontally across the images. 2nd row: Coronal slices of the XCAT phantoms (attenuation and activity overlaid) obtained from this MRI dataset. 3rd row: Difference images of XCAT attenuation between the 1st column and 1st - 4th columns showing the extent of respiratory motion. 4th row: Rendered XCAT phantoms. The sternum is displayed as semi-transparent to allow better visualization of the heart.

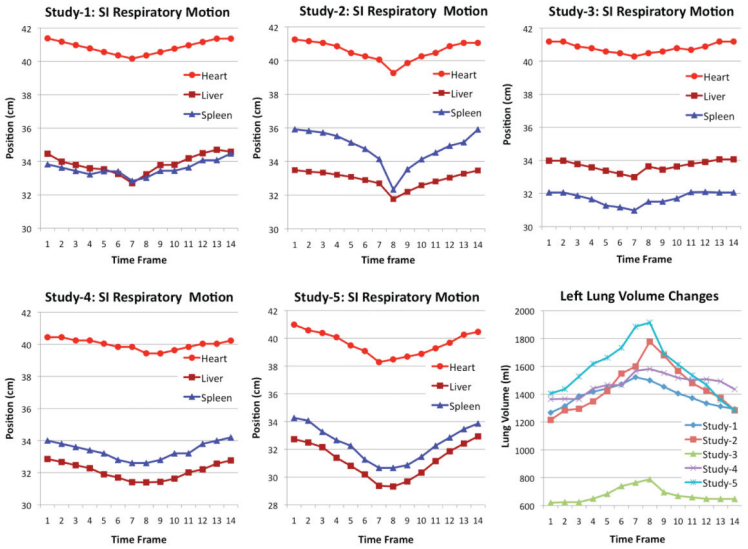

Figure 6.

Heart, liver and spleen SI-positions (relative to the lowest part of the phantom) obtained from the XCAT respiratory phantoms (14 frames each) based on the 5 volunteer studies. Also, in the bottom right corner, volume changes of the left lungs are shown for these studies. A similar trend was observed for the right lung volume changes (not shown).

Table 1

6-DOF body motions for the heart, liver, and spleen relative to their positions in the baseline pose for five volunteers in five poses

		AXIAL SLIDE			LATERAL BEND			SHOULDER TWIST			SHOULDER STRECH			SIDE ROLL		
#		Heart	Liver	Spleen	Heart	Liver	Spleen	Heart	Liver	Spleen	Heart	Liver	Spleen	Heart	Liver	Spleen
1	RL	− 1.0	− 0.2	0.1	3.9	15.1	14.7	16.3	24.8	27.7	5.6	8.5	9.7	3.2	7.7	8.9
	AP	2.0	0.3	0.0	2.1	− 2.5	− 3.9	5.7	− 0.7	4.6	4.0	− 0.8	3.9	6.1	− 1.3	1.9
	SI	− 17.0	− 15.1	− 16.7	− 10.9	− 16.8	− 1.9	− 2.3	− 6.2	− 0.7	3.0	− 5.8	2.7	− 0.1	− 1.8	− 5.2
	α	0.4	1.7	0.5	1.1	1.4	−0.3	1.1	3.5	−1.1	0.6	1.2	0.4	0.6	0.4	1.0
	β	−0.5	0.2	−0.6	−11.1	−10.9	−4.6	−7.5	−4.8	−4.4	−2.6	−3.6	−0.8	−0.4	−0.5	−0.7
	γ	−0.1	0.2	−0.6	−0.2	−1.7	0.9	−2.7	−3.6	2.1	−2.5	−2.5	0.5	−2.6	−3.0	0.8
2	RL	− 0.1	0.1	0.1	19.9	19.7	20.1	18.9	18.6	19.2	1.9	− 0.1	0.8	7.9	16.7	21.6
	AP	− 1.9	0.0	− 0.1	− 6.0	− 11.8	− 7.7	0.0	− 6.4	− 9.8	1.0	− 2.3	− 0.7	3.0	− 6.7	10.8
	SI	− 3.2	− 4.8	− 5.0	1.7	2.3	2.3	4.0	0.7	9.5	− 1.3	2.6	0.5	7.7	3.1	6.1
	α	0.7	0.0	−0.1	1.2	−0.2	0.0	0.2	−0.7	−0.6	1.4	0.0	−0.9	3.3	0.7	1.2
	β	−0.7	−0.1	−0.3	−0.8	−0.7	−0.7	−0.5	−1.4	0.1	−1.0	0.5	0.4	−5.9	−4.3	−2.8
	γ	1.9	0.0	−0.2	−0.7	−1.0	−0.6	−0.1	−2.2	−0.1	−0.8	−0.4	−0.8	−9.2	−8.1	−1.6
3	RL	3.9	4.1	4.2	22.4	29.3	23.5	8.1	15.4	12.9	7.9	8.1	7.6	3.3	10.1	14.1
	AP	− 2.1	− 2.2	− 2.5	− 2.0	1.5	4.1	− 1.8	1.7	1.6	0.0	0.1	0.1	3.9	1.5	6.1
	SI	− 22.1	− 21.0	− 22.3	6.0	− 10.7	− 9.4	− 5.1	− 9.3	− 7.0	3.9	2.1	− 1.9	− 0.1	− 12.3	0.6
	α	0.0	0.0	0.0	0.5	0.6	1.8	−4.3	−4.3	−1.6	−0.2	−0.1	0.4	0.3	−2.0	0.6
	β	0.7	0.1	0.6	−7.5	−4.9	−3.4	−1.9	−2.0	−0.9	0.5	−0.1	−0.3	0.1	4.0	−0.4
	γ	−0.2	−0.3	0.8	0.0	−3.6	2.1	0.0	−1.3	1.1	0.1	−0.6	0.3	−2.5	−3.2	0.2
4	RL	2.4	− 0.2	4.5	0.4	− 6.6	2.6	2.0	− 1.6	1.9	0.0	0.0	0.0	1.4	− 11.6	3.6
	AP	6.8	9.4	8.9	7.4	8.4	9.6	4.3	5.1	4.3	2.3	2.2	2.3	2.0	2.1	1.1
	SI	− 25.9	− 25.9	− 25.5	− 2.6	− 1.8	− 2.8	− 6.7	− 3.3	− 0.8	− 0.7	− 0.7	3.3	− 6.6	− 14.5	− 4.4
	α	0.6	−0.1	0.3	0.4	0.0	1.0	0.5	0.1	0.5	0.0	−0.2	0.6	0.4	0.0	0.2
	β	−0.7	−0.2	1.1	2.1	1.7	0.1	−0.3	0.4	0.0	0.2	0.0	−0.1	−2.9	−2.8	−1.0
	γ	2.1	2.2	1.1	4.3	4.3	2.0	−0.4	−0.1	0.5	−0.1	−0.3	0.7	4.3	4.5	1.2
5	RL	− 10.1	− 9.9	− 9.7	− 9.0	− 8.4	− 9.7	− 14.1	− 15.7	− 16.8	− 0.1	1.3	2.1	− 23.6	− 32.4	− 27.4

		AXIAL SLIDE			LATERAL BEND			SHOULDER TWIST			SHOULDER STRECH			SIDE ROLL		
#		Heart	Liver	Spleen	Heart	Liver	Spleen	Heart	Liver	Spleen	Heart	Liver	Spleen	Heart	Liver	Spleen
	AP	**0.0**	**0.0**	**0.1**	**− 3.2**	**0.8**	**− 4.7**	**− 4.4**	**1.5**	**− 9.3**	**0.0**	**− 2.1**	**− 0.1**	**− 0.5**	**6.8**	**− 1.9**
	SI	**− 25.3**	**− 25.0**	**− 25.1**	**− 7.7**	**− 9.3**	**− 9.3**	**− 2.2**	**− 5.3**	**− 3.0**	**− 4.2**	**− 5.2**	**0.0**	**− 7.8**	**− 6.8**	**− 14.9**
	α	0.2	−0.2	−0.1	0.2	−0.7	0.3	0.1	−0.7	−1.0	0.0	−0.4	0.2	0.0	−0.1	−2.3
	β	−0.2	0.0	−0.3	4.3	0.0	0.4	−0.2	−0.4	1.3	−0.2	−0.8	−1.0	4.5	3.9	0.8
	γ	−0.2	−0.1	−0.7	2.1	1.8	0.1	4.4	3.7	−0.5	0.0	−1.4	−0.4	5.7	4.4	−1.9

The 6-DOF motions in mm (bold font) and degrees (regular font) are: RL (translation in Right-Left), AP (translation in Anterior-Posterior) and SI (translation in Superior-Inferior), α (rotation about RL axis), β (rotation about AP axis) and γ (rotation about SI axis). Note motions are compared to a single baseline to which the volunteer approximately returned after completion of each requested motion. Thus motions listed other than for the first one completed after the baseline study are a mix of the motion requested and volunteers not returning exactly to baseline prior to performing subsequent motions.